

RESEARCH ARTICLE | APRIL 26 2024

Atomic layer molecular beam epitaxy of kagome magnet RMn_6Sn_6 (R = Er, Tb) thin films

Special Collection: [Spin-Related Quantum Materials and Devices](#)

Shuyu Cheng ; Binzhi Liu ; Igor Lyalin ; Wenyi Zhou ; Jinwoo Hwang ; Roland K. Kawakami  



APL Mater. 12, 041129 (2024)

<https://doi.org/10.1063/5.0182595>



APL Machine Learning

2023 Papers with Best Practices in Data Sharing and Comprehensive Background

[Read Now](#)



Atomic layer molecular beam epitaxy of kagome magnet RMn_6Sn_6 (R = Er, Tb) thin films

Cite as: APL Mater. 12, 041129 (2024); doi: 10.1063/5.0182595

Submitted: 19 October 2023 • Accepted: 9 April 2024 •

Published Online: 26 April 2024



Shuyu Cheng,¹  Binzhi Liu,²  Igor Lyalin,¹  Wenyi Zhou,¹  Jinwoo Hwang,^{2,a)} 
and Roland K. Kawakami^{1,b)} 

AFFILIATIONS

¹Department of Physics, The Ohio State University, Columbus, Ohio 43210, USA

²Department of Materials Science and Engineering, The Ohio State University, Columbus, Ohio 43210, USA

Note: This paper is part of the Special Topic on Spin-Related Quantum Materials and Devices.

^{a)}Electronic mail: hwang.458@osu.edu

^{b)}Author to whom correspondence should be addressed: kawakami.15@osu.edu

ABSTRACT

Kagome lattices have garnered substantial interest because their band structure consists of topological flat bands and Dirac cones. The RMn_6Sn_6 (R = rare earth) compounds are particularly interesting because of the existence of the large intrinsic anomalous Hall effect (AHE), which originates from the gapped Dirac cones near the Fermi level. This makes RMn_6Sn_6 an outstanding candidate for realizing the high-temperature quantum AHE. The growth of RMn_6Sn_6 thin films is beneficial for both fundamental research and potential applications. However, most of the studies on RMn_6Sn_6 have focused on bulk crystals, and the synthesis of RMn_6Sn_6 thin films has not been reported so far. Here, we report the atomic layer molecular beam epitaxy growth, structural and magnetic characterizations, and transport properties of ErMn_6Sn_6 and TbMn_6Sn_6 thin films. It is especially noteworthy that TbMn_6Sn_6 thin films have out-of-plane magnetic anisotropy, which is important for realizing the quantum AHE. Our work paves the avenue toward the control of the AHE using devices patterned from RMn_6Sn_6 thin films.

© 2024 Author(s). All article content, except where otherwise noted, is licensed under a Creative Commons Attribution (CC BY) license (<https://creativecommons.org/licenses/by/4.0/>). <https://doi.org/10.1063/5.0182595>

Materials with layered kagome structures provide an ideal platform for studying the interplay between the band structure and magnetism. In momentum space, a two-dimensional kagome lattice manifests Dirac cones at the K points,^{1,2} saddle points at the M points,^{3,4} and a flat band across the Brillouin zone.^{5,6} The introduction of magnetism and spin-orbital coupling further opens a gap at the band touching points, leading to topologically non-trivial electronic states.^{7–9} In the real space, non-trivial spin textures (e.g., magnetic skyrmions) have been observed in kagome magnets.^{10,11}

Recently, RMn_6Sn_6 (R = rare earth) compounds have emerged as a new family of topological kagome magnets.^{12,13} The Mn atoms in RMn_6Sn_6 form the Mn_3 kagome layers and the spin ordering of the Mn_3 layers is largely affected by the R atoms. Previous studies on bulk crystals report that R = Gd, Tb, Dy, and Ho give rise to ferromagnetic coupling of Mn spins, while R = Er, Tm, and Lu lead to antiferromagnetic coupling of Mn spins at zero field.^{14–16} Rare earth elements in RMn_6Sn_6 compounds also provide one additional knob for simultaneously tuning the magnetocrystalline anisotropy (MCA) and the band structure, more specifically, the position and

the gap opening of the Dirac cones.¹³ The large Berry-curvature-induced intrinsic anomalous Hall effect (AHE) may originate from the gapped Dirac cones close to the Fermi level because the intrinsic anomalous Hall conductivity (AHC) is connected to the Dirac gap opening Δ and the Dirac cone position E_D through¹⁷

$$\sigma^{int} = \frac{e^2}{h} \frac{\Delta}{2E_D}. \quad (1)$$

Notably, TbMn_6Sn_6 bulk crystals exhibit out-of-plane (OOP) magnetic anisotropy, which leads to a 34 meV Dirac gap opening at 130 meV above the Fermi level,¹² and band structure calculations predict the quantum anomalous Hall effect (QAHE) if the Fermi level could be tuned into the gap. Experimentally, the observation of a giant intrinsic AHC of $\sigma^{int} = 0.14 e^2/h$ per kagome layer in TbMn_6Sn_6 bulk crystals¹² makes the RMn_6Sn_6 family of materials attractive for QAHE. To this end, the growth of RMn_6Sn_6 thin films provides opportunities for tuning the band structure and the Fermi level through epitaxial strain, chemical doping, or voltage gating.

However, all the reported studies have focused on bulk crystals of RMn_6Sn_6 , while studies on their thin film counterparts have been missing. Therefore, the development of epitaxial RMn_6Sn_6 thin films is highly desired.

In this paper, we report the growth of (0001)-oriented thin films of ErMn_6Sn_6 and TbMn_6Sn_6 using atomic layer molecular beam epitaxy (AL-MBE) and characterize their magnetic and transport properties. The films are grown on Pt(111) buffer layers on $\text{Al}_2\text{O}_3(0001)$ substrates. Various methods are employed to characterize the structure of our samples, including *in situ* reflection high energy electron diffraction (RHEED), x-ray diffraction (XRD), atomic force microscopy (AFM), and scanning transmission electron microscopy (STEM). We demonstrate that the magnetic properties of RMn_6Sn_6 thin films can be tuned through the selection of the rare earth element R . ErMn_6Sn_6 thin films favor in-plane (IP) magnetization, while TbMn_6Sn_6 thin films undergo an out-of-plane (OOP) magnetization to IP spin-reorientation transition (SRT) as the temperature increases above 300 K. Finally, we find that the longitudinal resistance of $\text{RMn}_6\text{Sn}_6/\text{Pt}$ bilayers does not follow a simple parallel resistor model but instead depends on the electron mean free path and can be explained qualitatively by the Fuchs-Sondheimer model.

The crystal structure of RMn_6Sn_6 is shown in Fig. 1, featuring a hexagonal lattice (space group $P6/mmm$, lattice constants $a = 5.5 \text{ \AA}$, and $c = 9.0 \text{ \AA}$) with atomic layers stacked along the c axis.¹⁸ In each unit cell, there are two kagome Mn_3 layers closely neighbored by two Sn_1 layers, with one honeycomb Sn_2 layer inserted between two Sn_1 layers and one RSn_2 layer inserted between Mn_3 kagome layers. Inspired by this stacking sequence, we develop an AL-MBE recipe to grow ErMn_6Sn_6 and TbMn_6Sn_6 thin films on epitaxial Pt(111) buffer layers on $\text{Al}_2\text{O}_3(0001)$ substrates. In AL-MBE, atomic layers are grown sequentially by opening and closing the appropriate MBE source shutters with precise timing. A similar growth strategy allowed us to synthesize thin films of another kagome magnet, Fe_3Sn_2 , which also has a hexagonal layered lattice structure.¹⁹

The base pressure of the growth chamber is 1×10^{-9} Torr. The $\text{Al}_2\text{O}_3(0001)$ substrates (MTI corporation) are annealed in air at 1000°C for 3 h and then degassed *in situ* at 500°C for 30 min to prepare a flat and clean surface. A 5 nm epitaxial Pt(111) buffer layer is subsequently grown on $\text{Al}_2\text{O}_3(0001)$ following the recipe described in our previous work.¹⁹ The $\text{ErMn}_6\text{Sn}_6(0001)$ and $\text{TbMn}_6\text{Sn}_6(0001)$ thin films are grown on Pt(111) buffer layers at 100 and 80°C , respectively, using the AL-MBE recipe described below. We note that the same heater power (9 W) was used for both the samples, and we attribute the different thermocouple temperatures to a drift in the temperature calibration between the ErMn_6Sn_6 and TbMn_6Sn_6 samples grown several months apart. For AL-MBE, the kagome Mn_3 layer and hexagonal Sn_1 layer are co-deposited with the flux ratio $\text{Mn}:\text{Sn} = 3:1$; the honeycomb RSn_2 is deposited with the flux ratio $\text{Er}:\text{Sn}$ (or $\text{Tb}:\text{Sn}$) = 2:1; another hexagonal Sn_1 layer and kagome Mn_3 layer are co-deposited; and then, one Sn_2 layer is deposited. The aforementioned shutter growth sequence is repeated until the desired thickness (typically 20 nm) of RMn_6Sn_6 is achieved. Typical deposition rates are 1.6, 1.6, 3.9, and $2.8 \text{ \AA}/\text{min}$ for Er, Tb, Mn, and Sn, respectively. After growth, a 5 nm CaF_2 layer is deposited to prevent sample oxidation.

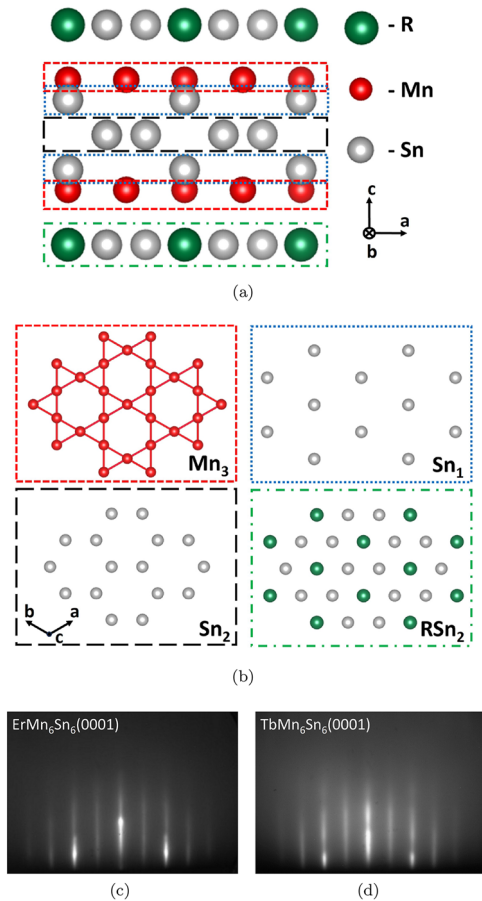


FIG. 1. AL-MBE growth of RMn_6Sn_6 thin films. (a) Lattice structure of RMn_6Sn_6 viewed from the side. In each unit cell, RMn_6Sn_6 consists of alternating stacking of RSn_2 , Mn_3 , Sn_1 , Sn_2 , Sn_1 , Mn_3 layers (from bottom to top) along the c axis. (b) In-plane lattice structure of kagome Mn_3 (top left), triangular Sn_1 (top right), honeycomb Sn_2 (bottom left), and RSn_2 (bottom right) layers. (c) *In situ* RHEED pattern of 20 nm ErMn_6Sn_6 sample grown on the Pt(111) buffer layer on the $\text{Al}_2\text{O}_3(0001)$ substrate. (d) *In situ* RHEED pattern of 20 nm TbMn_6Sn_6 sample grown on the Pt(111) buffer layer on the $\text{Al}_2\text{O}_3(0001)$ substrate.

The *in situ* RHEED patterns of ErMn_6Sn_6 and TbMn_6Sn_6 are monitored during the growth. The RHEED patterns of a 20 nm ErMn_6Sn_6 thin film and a 20 nm TbMn_6Sn_6 thin film along $\text{Al}_2\text{O}_3[11\bar{2}0]$ direction are shown in Figs. 1(c) and 1(d), respectively. The RHEED patterns are generally streaky, suggesting that the morphology of our RMn_6Sn_6 thin films is dominated by two-dimensional terraces with finite sizes, although some three-dimensional features also exist as spots. The RHEED pattern suggests that the in-plane lattice constants for our samples are $a_{\text{ErMn}_6\text{Sn}_6} = 5.47 \text{ \AA}$, and $a_{\text{TbMn}_6\text{Sn}_6} = 5.56 \text{ \AA}$, respectively, and the in-plane epitaxial relationship is $\text{RMn}_6\text{Sn}_6[1\bar{1}00] \parallel \text{Pt}[11\bar{2}] \parallel \text{Al}_2\text{O}_3[11\bar{2}0]$.

We perform XRD measurements to confirm the crystallographic structures of the ErMn_6Sn_6 and TbMn_6Sn_6 thin films. The x ray is from the Cu-K α radiation, with a wavelength of 1.5406 \AA . Figure 2(a) shows the XRD data of a 20 nm ErMn_6Sn_6 thin film. Next to the substrate peaks at 41.57° and 90.60° , two major

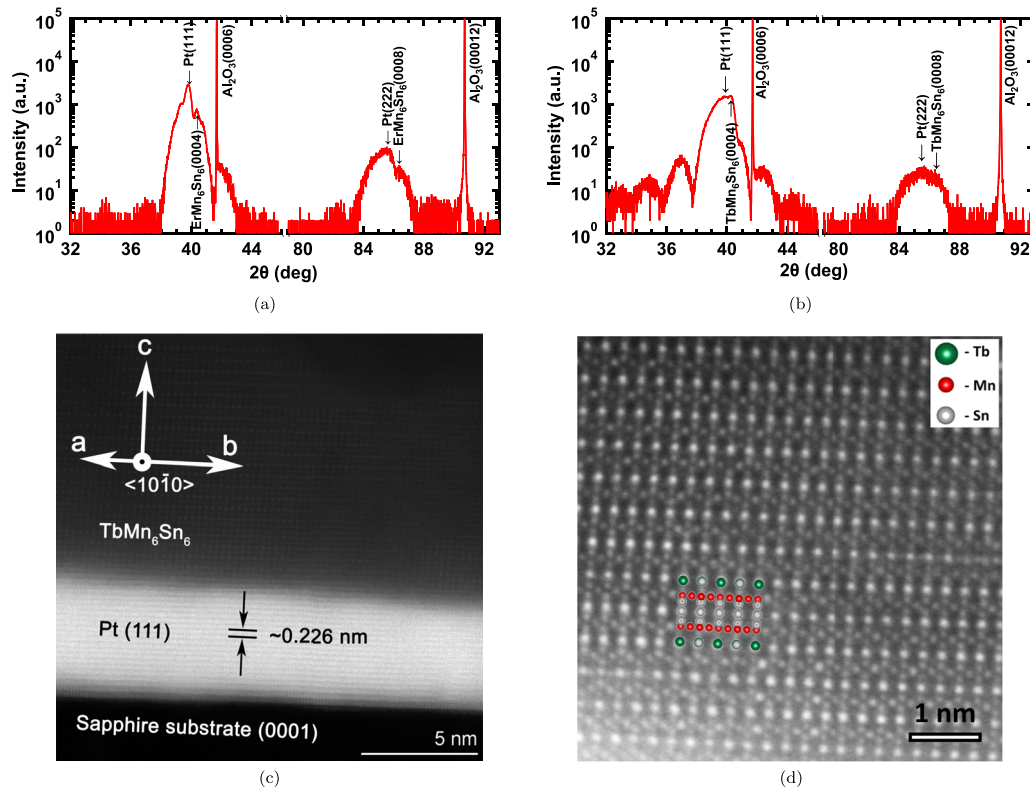


FIG. 2. Structural characterizations of the RMn_6Sn_6 thin films. (a) XRD data of an $\text{ErMn}_6\text{Sn}_6(20\text{ nm})/\text{Pt}(5\text{ nm})$ sample. (b) XRD data of a $\text{TbMn}_6\text{Sn}_6(25\text{ nm})/\text{Pt}(5\text{ nm})$ sample. (c) STEM-HAADF image of $\text{TbMn}_6\text{Sn}_6(0001)/\text{Pt}(111)$ taken near the interface, showcasing the cross section of a TbMn_6Sn_6 film with crystal orientation along the $[10\bar{1}0]$ direction. (d) A zoomed-in STEM-HAADF image with the model of the TbMn_6Sn_6 lattice overlaid on top.

peaks are found at 39.78° and 85.46° , respectively. These peaks are attributed to the Pt(111) and Pt(222) peaks because their 2θ angles convert to out-of-plane lattice constants of 2.275 and 2.270 Å, respectively. These values are close to the out-of-plane lattice constant of Pt along the (111) direction ($\sqrt{3}/3 \times 3.923\text{ Å} = 2.265\text{ Å}$).²⁰ The $\text{ErMn}_6\text{Sn}_6(0004)$ and $\text{ErMn}_6\text{Sn}_6(0008)$ peaks appear as nearby shoulder peaks at 40.36° and 87.63° , respectively. The out-of-plane lattice constant of ErMn_6Sn_6 extracted from the (0004) peak is 8.93 Å, which is close to, but slightly smaller than, the reported bulk value of 9.0006 Å.²¹

For TbMn_6Sn_6 thin film, the general characteristics of the XRD data are similar to ErMn_6Sn_6 . To the right of the Pt(111) peak, which is at 39.66° , the $\text{TbMn}_6\text{Sn}_6(0004)$ peak is found as a shoulder peak [see Fig. 2(b)]. A double Gaussian peak fitting (see the supplementary material, S1) yields the $\text{TbMn}_6\text{Sn}_6(0004)$ peak position of 40.25° , which corresponds to an out-of-plane lattice of $c = 8.96\text{ Å}$. This is also smaller than the reported bulk value of 9.0208 Å.²¹

We characterize the surface morphology of ErMn_6Sn_6 and TbMn_6Sn_6 thin films using AFM. The AFM images are displayed in the supplementary material S2. Both ErMn_6Sn_6 and TbMn_6Sn_6 thin films have continuous and flat surfaces with sub-micrometer grain

sizes. The root-mean-square (rms) roughness is 1.02 nm for a 20 nm ErMn_6Sn_6 thin film and 1.45 nm for a 20 nm TbMn_6Sn_6 sample, respectively.

We perform cross-sectional STEM measurements on a TbMn_6Sn_6 thin film along the $\text{Al}_2\text{O}_3[11\bar{2}0]$ direction (see the supplementary material, S3 for details). Figure 2(c) shows the STEM high-angle annular dark-field (HAADF) image taken near the $\text{TbMn}_6\text{Sn}_6/\text{Pt}$ interface. The spacing between the two Pt(111) atomic layers is determined to be $\sim 0.226\text{ nm}$, consistent with the previously reported value on bulk crystals.²² It can be concluded from the STEM image that the TbMn_6Sn_6 is epitaxially grown on the Pt(111) buffer layer along the c axis, with the in-plane epitaxial relationship of $\text{TbMn}_6\text{Sn}_6[1\bar{1}00] \parallel \text{Pt}[11\bar{2}] \parallel \text{Al}_2\text{O}_3[11\bar{2}0]$. A sharp interface between TbMn_6Sn_6 and Pt is observed, with very limited interdiffusion. A zoomed-in STEM-HAADF image is shown in Fig. 2(d), with the model of the TbMn_6Sn_6 lattice overlaid on top. The brighter dots are identified as Tb and Sn atoms due to their larger atomic numbers. The TbSn_2 layers and Sn_2 layers appear to be nearly identical in the STEM image, and we attribute this to the stacking fault or a lattice offset inherited from the atomic steps of the Pt(111) buffer layer.

To investigate the magnetic properties of the RMn_6Sn_6 thin films, we obtain superconducting quantum interference device

(SQUID) magnetometer measurements. Figure 3(a) shows the IP (blue) and OOP (red) hysteresis loops of a 20 nm ErMn_6Sn_6 thin film. The IP hysteresis loop has a smaller saturation field of 0.2 T, while the OOP hysteresis loop has a larger saturation field of 1.7 T, indicating that ErMn_6Sn_6 has easy-plane anisotropy at room temperature. The saturation magnetization of ErMn_6Sn_6 thin film is $5.4 \mu_B/\text{f.u.}$ (212 kA/m) at room temperature. The IP and OOP hysteresis loops of ErMn_6Sn_6 at $T = 5$ K are shown in Fig. 3(b). At $T = 5$ K, both IP and OOP hysteresis loops show much larger coercive fields and larger saturation fields, while the saturation field of the OOP hysteresis loop is still larger than the IP hysteresis loop. The IP loop exhibits a sharper switching behavior, with the coercive field of 0.47 T. Meanwhile, the OOP hysteresis loop becomes narrower near zero fields and wider at higher fields. The coercive field of the OOP hysteresis loop is 0.30 T.

We measure the temperature-dependence of remanent magnetization of the ErMn_6Sn_6 thin film, as shown in Fig. 3(c). For both OOP (the red curve) and IP (the blue curve) measurements, the sample is cooled down in a 7 T applied field, and measured at low field while heating up. A 30 mT field is applied to maintain the polarity of the magnetization. From the temperature-dependent magnetization curve, the Curie temperature of the 20 nm ErMn_6Sn_6 thin film is determined to be 353 K, signified by a drop of magnetization to zero. This Curie temperature is consistent with the reported value of 350 K on ErMn_6Sn_6 bulk crystals.¹⁶

Compared to ErMn_6Sn_6 thin films, TbMn_6Sn_6 thin films show different magnetic properties. Figures 3(d) and 3(e) show the hysteresis loops of a 25 nm TbMn_6Sn_6 thin film at 300 and 5 K, respectively. At $T = 300$ K, the OOP (red) and IP (blue) hysteresis

loops of TbMn_6Sn_6 are almost identical, with a saturation field of 0.6 T [see Fig. 3(d)]. The saturation magnetization of TbMn_6Sn_6 is $3.9 \mu_B/\text{f.u.}$ (154 kA/m) at room temperature. While cooling down to $T = 5$ K, the OOP hysteresis loop of TbMn_6Sn_6 exhibits a square shape, with tails extended to 5 T, as shown in Fig. 3(e). Meanwhile, the IP hysteresis loop shows a gradual switching behavior. At zero field, the OOP remanent magnetization is much larger than the IP remanent magnetization, suggesting that TbMn_6Sn_6 favors OOP at $T = 5$ K.

The perpendicular magnetic anisotropy is highly unusual for epitaxial kagome magnet thin films, as most of the previously reported kagome magnet thin films have had easy-plane anisotropy.^{19,23–27} Even for epitaxial Fe_3Sn_2 whose bulk form has MCA along the c axis, the MCA is overcome by the magnetic shape anisotropy (MSA), which favors easy-plane anisotropy. As a result, both MBE-grown and sputtered Fe_3Sn_2 thin films manifest easy-plane anisotropy.^{19,25} However, in TbMn_6Sn_6 thin films, the MCA is strong enough to overcome the MSA and leads to an easy-axis anisotropy at low temperatures. It is noteworthy that such large magnetocrystalline anisotropy along the c axis opens a gap at the Dirac cone, leading to a large intrinsic AHE.^{12,13}

The perpendicular magnetic anisotropy of the TbMn_6Sn_6 thin film sample at low temperatures is further confirmed by the temperature-dependent SQUID measurements, as shown in Fig. 3(f). After field cooling, a 20 mT field is applied to maintain the polarity of the magnetization. Below 300 K, the OOP magnetization (red curve) is always larger than the IP magnetization (blue curve). A crossover between IP and OOP magnetization happens at $T = 300$ K, above which the IP magnetization becomes larger than the OOP

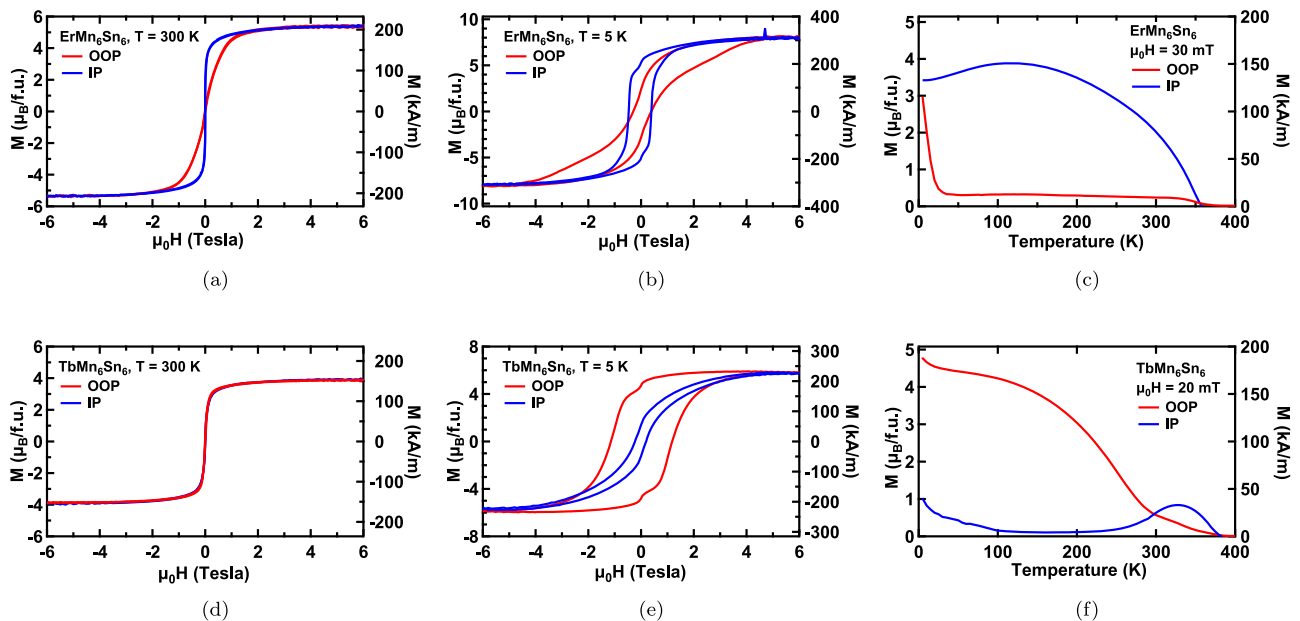


FIG. 3. Magnetic properties of ErMn_6Sn_6 and TbMn_6Sn_6 thin films. (a)–(c) Magnetic properties of 20 nm ErMn_6Sn_6 thin film measured with out-of-plane (OOP, red) and in-plane (IP, blue) geometries. (a) M vs H hysteresis loops measured at $T = 300$ K. (b) M vs H hysteresis loop measured at $T = 5$ K. (c) M vs T curve. (d)–(f) Magnetic properties of 25 nm TbMn_6Sn_6 thin film measured with out-of-plane (OOP, red) and in-plane (IP, blue) geometries. (d) M vs H hysteresis loops measured at $T = 300$ K. (e) M vs H hysteresis loop measured at $T = 5$ K. (f) M vs T curve, showing uniaxial anisotropy for $T < 300$ K and an OOP-to-IP spin reorientation at $T = 300$ K.

magnetization. This crossover suggests an OOP-to-IP SRT as the temperature increases above 300 K. A similar temperature-induced SRT has been observed at 310 K in TbMn_6Sn_6 bulk crystals¹⁶ and is reported to be related to the formation of magnetic skyrmions.¹¹ Both IP and OOP magnetization eventually disappears above the Curie temperature, which is determined to be 380 K. This Curie temperature is lower than the reported value of 423 K on TbMn_6Sn_6 bulk crystals.¹⁴

Next, we discuss the transport properties of $\text{ErMn}_6\text{Sn}_6/\text{Pt}$ and $\text{TbMn}_6\text{Sn}_6/\text{Pt}$ thin films. The transport measurements are performed using the Quantum Design Physical Property Measurement System (PPMS) on $300 \times 100 \mu\text{m}^2$ Hall bar devices patterned from $\text{ErMn}_6\text{Sn}_6/\text{Pt}$ and $\text{TbMn}_6\text{Sn}_6/\text{Pt}$ thin films. The longitudinal resistance of the Hall bar devices at zero field is shown in Fig. 4(a). Comparing between the $\text{TbMn}_6\text{Sn}_6(25 \text{ nm})/\text{Pt}(5 \text{ nm})$ bilayer (the red curve) and $\text{Pt}(5 \text{ nm})$ single layer (the black dashed curve), the bilayer resistance is lower than the Pt single layer resistance for higher temperatures ($T > 200 \text{ K}$). This is consistent with the parallel resistor model in which the TbMn_6Sn_6 and Pt layers are modeled as two resistors connected in parallel and, therefore, have smaller resistance than the Pt layer alone. The parallel resistor model has been widely used to extract the resistivity of kagome material thin films grown on metallic buffer layers.^{24–26,28} However, at low temperatures ($T < 150 \text{ K}$), the resistance of the $\text{TbMn}_6\text{Sn}_6(25 \text{ nm})/\text{Pt}(5 \text{ nm})$ bilayer is larger than that of the $\text{Pt}(5 \text{ nm})$ single layer. This is the opposite of what one would expect from the parallel resistor model. The comparison between the $\text{ErMn}_6\text{Sn}_6(20 \text{ nm})/\text{Pt}(5 \text{ nm})$ bilayer (the green curve) and $\text{Pt}(5 \text{ nm})$ single layer shows a similar trend that the bilayer resistance is smaller than the Pt single layer resistance for $T > 200 \text{ K}$ and is larger than the Pt single layer resistance for $T < 100 \text{ K}$. The deviation from the parallel resistor model is more pronounced for the bilayers with smaller kagome layer thicknesses. For example, for the $\text{TbMn}_6\text{Sn}_6(5 \text{ nm})/\text{Pt}(5 \text{ nm})$ bilayer (the blue curve), the resistance is larger than that of the $\text{Pt}(5 \text{ nm})$ single layer from $T = 5 \text{ K}$ up to $T = 300 \text{ K}$.

The deviation from the parallel resistor model can be explained by the Fuchs-Sondheimer theory, in which the resistance of bilayers depends not only on the bulk resistance of two materials but also on the mean free path of electrons in them.^{29,30} In the Fuchs-Sondheimer model, when the electron mean free path is much smaller than the thickness of each layer, the bilayer resistance is smaller than the resistance of individual layers. In this case, the Fuchs-Sondheimer model converges to the parallel resistor model. However, when the electron mean free path is much larger than the thickness of each layer, the bilayer resistance is larger than the resistance of individual layers, which is more similar to the series resistor model. Especially in an infinite superlattice consisting of alternating stacking of two materials with the same thickness, in the thin layer limit and under the assumption that the electron densities in two materials are identical, the averaged resistivity of the superlattice is exactly equal to the average value of the bulk resistivity of the two materials.³¹ In our $\text{RMn}_6\text{Sn}_6/\text{Pt}$ bilayer samples, the scattering length is shorter than the individual layer thickness at high temperatures; therefore, the bilayer resistance is smaller than the resistance of Pt layer, similar to the parallel resistor model. Meanwhile, at low temperatures or with smaller thicknesses, the mean free path becomes longer than the individual layer thickness, and the bilayer resistance is

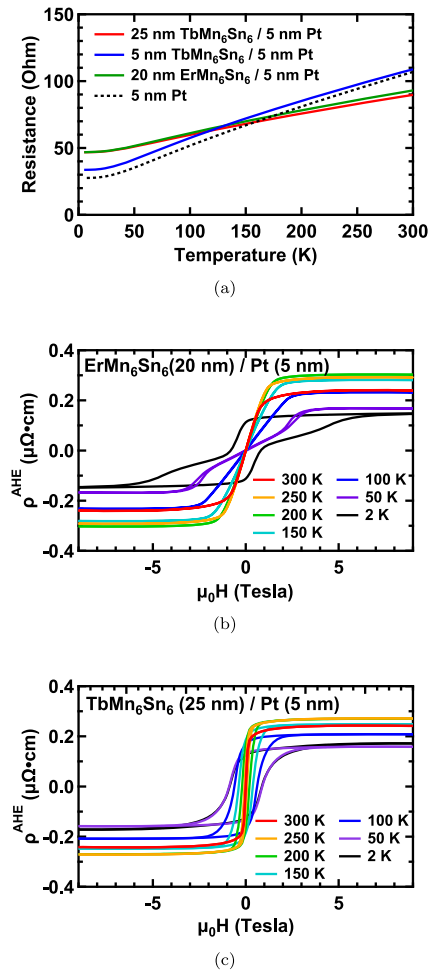


FIG. 4. Transport measurements of $\text{ErMn}_6\text{Sn}_6/\text{Pt}$ and $\text{TbMn}_6\text{Sn}_6/\text{Pt}$ bilayers. (a) Resistance of $300 \times 100 \mu\text{m}^2$ devices patterned from the $\text{TbMn}_6\text{Sn}_6(25 \text{ nm})/\text{Pt}(5 \text{ nm})$ bilayer (red), $\text{TbMn}_6\text{Sn}_6(5 \text{ nm})/\text{Pt}(5 \text{ nm})$ bilayer (blue), $\text{ErMn}_6\text{Sn}_6(20 \text{ nm})/\text{Pt}(5 \text{ nm})$ bilayer, and 5 nm Pt single layer (black dashed), respectively. (b) Anomalous Hall resistivity of the $\text{ErMn}_6\text{Sn}_6(20 \text{ nm})/\text{Pt}(5 \text{ nm})$ bilayer measured at different temperatures ranging from 2 to 300 K. (c) Anomalous Hall resistivity of the $\text{TbMn}_6\text{Sn}_6(25 \text{ nm})/\text{Pt}(5 \text{ nm})$ bilayer measured at different temperatures ranging from 2 to 300 K.

larger than the resistance of Pt layer, similar to the series resistor model.

We also measured the anomalous Hall effect (AHE) of the $\text{ErMn}_6\text{Sn}_6(20 \text{ nm})/\text{Pt}(5 \text{ nm})$ and $\text{TbMn}_6\text{Sn}_6(25 \text{ nm})/\text{Pt}(5 \text{ nm})$ bilayers, as shown in Figs. 4(b) and 4(c), respectively. Here, the anomalous Hall resistivity is calculated by multiplying the anomalous Hall resistance by the thickness of the RMn_6Sn_6 layer. The native AHE resistivity of the RMn_6Sn_6 layer is expected to be larger at higher temperatures due to the parallel conductance from the Pt buffer layer. However, due to the complexity of data analysis, extracting the intrinsic transport coefficients of ErMn_6Sn_6 and TbMn_6Sn_6 is outside the scope of this paper. For ErMn_6Sn_6 , the AHE hysteresis loop at $T = 2 \text{ K}$ has a large remanence, a low-field opening (with the coercive field of $\sim 1 \text{ T}$), and a large saturation field ($\sim 6 \text{ T}$). The opening

of the hysteresis loop decreases quickly as the temperature increases and almost disappears before the temperature reaches 100 K. For TbMn_6Sn_6 , the AHE hysteresis loops are relatively square, with the coercive field decreasing as the temperature increases. For both materials, as the temperature increases from 2 to 300 K, the amplitude of AHE first increases, reaches the maximum value between 200 and 250 K, and then decreases. This behavior is understood as follows: the anomalous Hall resistivity ρ^{AH} scales with ρ_{xx}^α , where α is between 1 and 2. The intrinsic and side-jump contributions yield $\alpha = 2$ and skew-scattering yields $\alpha = 1$.³² Since ρ_{xx} increases with the temperature [Fig. 4(a)], this scaling explains the enhancement of ρ^{AH} with temperature as observed below 200 K. On the other hand, the reduction in AHE resistivity at higher temperatures can be attributed to the decrease in magnetization as the temperature approaches the Curie temperature.

In conclusion, this study demonstrates the synthesis of *c*-plane ErMn_6Sn_6 and TbMn_6Sn_6 thin films using atomic layer molecular beam epitaxy. A combination of RHEED, XRD, AFM, and STEM confirms the structure of the samples. The magnetization measurements show that ErMn_6Sn_6 has easy-plane anisotropy from 5 K to room temperature, while TbMn_6Sn_6 has perpendicular magnetic anisotropy at low temperature and an OOP-to-IP spin reorientation as the temperature increases above 300 K. The transport measurements at low temperatures show that the longitudinal resistance of the $\text{RMn}_6\text{Sn}_6/\text{Pt}$ bilayer is larger than that of the Pt layer alone, which is inconsistent with the parallel resistance model. On the other hand, such behavior is qualitatively explained by the Fuchs-Sondheimer model. Finally, since both ErMn_6Sn_6 and TbMn_6Sn_6 are synthesized under similar conditions, other members of the RMn_6Sn_6 family could likely be grown using similar AL-MBE recipes. These results create a solid foundation for future research and applications based on RMn_6Sn_6 thin films.

See the supplementary material for additional XRD data of TbMn_6Sn_6 thin films, AFM images of ErMn_6Sn_6 and TbMn_6Sn_6 thin films, and technical details of STEM measurements.

We thank Daniel Halbing, Katherine Robinson, and Xueshi Gao for their assistance in the construction of the evaporation cells. S.C. was supported by the NSF Grant No. CHE-1935885. B.L. and I.L. were supported by the Center for Emergent Materials, an NSF MRSEC, under Grant No. DMR-2011876. W.Z. was supported by AFOSR MURI 2D MAGIC Grant No. FA9550-19-1-0390 and the U.S. Department of Energy Grant No. DE-SC0016379. The partial funding for shared facilities used in this research was provided by the Center for Emergent Materials, an NSF MRSEC, under Award No. DMR-2011876.

AUTHOR DECLARATIONS

Conflict of Interest

The authors have no conflicts to disclose.

Author Contributions

Shuyu Cheng: Conceptualization (equal); Investigation (lead); Writing – original draft (equal); Writing – review & editing (equal).

Binzhi Liu: Investigation (supporting); Writing – review & editing (equal). **Igor Lyalin:** Investigation (supporting); Writing – review & editing (equal). **Wenyi Zhou:** Investigation (supporting); Writing – review & editing (equal). **Jinwoo Hwang:** Supervision (equal); Writing – review & editing (equal). **Roland K. Kawakami:** Conceptualization (equal); Supervision (lead); Writing – original draft (equal); Writing – review & editing (equal).

DATA AVAILABILITY

The data that support the findings of this study are available from the corresponding author upon reasonable request.

REFERENCES

- K. Kuroda, T. Tomita, M.-T. Suzuki, C. Baille, A. Nugroho, P. Goswami, M. Ochi, M. Ikhlas, M. Nakayama, S. Akebi, R. Noguchi, R. Ishii, N. Inami, K. Ono, H. Kumigashira, A. Varykhalov, T. Muro, T. Koretsune, R. Arita, S. Shin, T. Kondo, and S. Nakatsuji, “Evidence for magnetic Weyl fermions in a correlated metal,” *Nat. Mater.* **16**, 1090–1095 (2017).
- L. Ye, M. Kang, J. Liu, F. Von Cube, C. R. Wicker, T. Suzuki, C. Jozwiak, A. Bostwick, E. Rotenberg, D. C. Bell, L. Fu, R. Comin, and J. G. Checkelsky, “Massive Dirac fermions in a ferromagnetic kagome metal,” *Nature* **555**, 638–642 (2018).
- M. Kang, S. Fang, J.-K. Kim, B. R. Ortiz, S. H. Ryu, J. Kim, J. Yoo, G. Sangiovanni, D. Di Sante, B.-G. Park, C. Jozwiak, A. Bostwick, E. Rotenberg, E. Kaxiras, S. D. Wilson, J.-H. Park, and R. Comin, “Twofold van Hove singularity and origin of charge order in topological kagome superconductor CsV_3Sb_5 ,” *Nat. Phys.* **18**, 301–308 (2022).
- X. Teng, J. S. Oh, H. Tan, L. Chen, J. Huang, B. Gao, J.-X. Yin, J.-H. Chu, M. Hashimoto, D. Lu, C. Jozwiak, A. Bostwick, E. Rotenberg, G. E. Granroth, B. Yan, R. J. Birgeneau, P. Dai, and M. Yi, “Magnetism and charge density wave order in kagome FeGe ,” *Nat. Phys.* **19**, 814 (2023).
- M. Kang, S. Fang, L. Ye, H. C. Po, J. Denlinger, C. Jozwiak, A. Bostwick, E. Rotenberg, E. Kaxiras, J. G. Checkelsky, and R. Comin, “Topological flat bands in frustrated kagome lattice CoSn ,” *Nat. Commun.* **11**, 4004 (2020).
- M. Kang, L. Ye, S. Fang, J.-S. You, A. Levitan, M. Han, J. I. Facio, C. Jozwiak, A. Bostwick, E. Rotenberg, M. K. Chan, R. D. McDonald, D. Graf, K. Kaznatcheev, E. Vescovo, D. C. Bell, E. Kaxiras, J. van den Brink, M. Richter, M. Prasad Ghimire, J. G. Checkelsky, and R. Comin, “Dirac fermions and flat bands in the ideal kagome metal FeSn ,” *Nat. Mater.* **19**, 163–169 (2020).
- K. Sun, Z. Gu, H. Katsura, and S. Das Sarma, “Nearly flatbands with nontrivial topology,” *Phys. Rev. Lett.* **106**, 236803 (2011).
- H.-M. Guo and M. Franz, “Topological insulator on the kagome lattice,” *Phys. Rev. B* **80**, 113102 (2009).
- A. Bolens and N. Nagaosa, “Topological states on the breathing kagome lattice,” *Phys. Rev. B* **99**, 165141 (2019).
- Z. Hou, W. Ren, B. Ding, G. Xu, Y. Wang, B. Yang, Q. Zhang, Y. Zhang, E. Liu, F. Xu, W. Wang, G. Wu, X. Zhang, B. Shen, and Z. Zhang, “Observation of various and spontaneous magnetic skyrmionic bubbles at room temperature in a frustrated kagome magnet with uniaxial magnetic anisotropy,” *Adv. Mater.* **29**, 1701144 (2017).
- Z. Li, Q. Yin, Y. Jiang, Z. Zhu, Y. Gao, S. Wang, J. Shen, T. Zhao, J. Cai, H. Lei, S.-Z. Lin, Y. Zhang, and B. Shen, “Discovery of topological magnetic textures near room temperature in quantum magnet TbMn_6Sn_6 ,” *Adv. Mater.* **35**, 2211164 (2023).
- J.-X. Yin, W. Ma, T. A. Cochran, X. Xu, S. S. Zhang, H.-J. Tien, N. Shumiya, G. Cheng, K. Jiang, B. Lian, Z. Song, G. Chang, I. Belopolski, D. Multer, M. Litskevich, Z.-J. Cheng, X. P. Yang, B. Swidler, H. Zhou, H. Lin, T. Neupert, Z. Wang, N. Yao, T.-R. Chang, S. Jia, and M. Zahid Hasan, “Quantum-limit Chern topological magnetism in TbMn_6Sn_6 ,” *Nature* **583**, 533–536 (2020).
- W. Ma, X. Xu, J.-X. Yin, H. Yang, H. Zhou, Z.-J. Cheng, Y. Huang, Z. Qu, F. Wang, M. Z. Hasan, and S. Jia, “Rare earth engineering in RMn_6Sn_6 ($R = \text{Gd-Tm, Lu}$) topological kagome magnets,” *Phys. Rev. Lett.* **126**, 246602 (2021).

- ¹⁴G. Venturini, B. C. El Idrissi, and B. Malaman, "Magnetic properties of RMn_6Sn_6 ($R = \text{Sc}, \text{Y}, \text{Gd-Tm}, \text{Lu}$) compounds with HfFe_6Ge_6 type structure," *J. Magn. Magn. Mater.* **94**, 35–42 (1991).
- ¹⁵B. Malaman, G. Venturini, R. Welter, J. Sanchez, P. Vulliet, and E. Ressouche, "Magnetic properties of RMn_6Sn_6 ($R = \text{Gd-Er}$) compounds from neutron diffraction and Mössbauer measurements," *J. Magn. Magn. Mater.* **202**, 519–534 (1999).
- ¹⁶D. M. Clatterbuck and K. A. Gschneidner, Jr., "Magnetic properties of RMn_6Sn_6 ($R = \text{Tb}, \text{Ho}, \text{Er}, \text{Tm}, \text{Lu}$) single crystals," *J. Magn. Magn. Mater.* **207**, 78–94 (1999).
- ¹⁷N. A. Sinitsyn, A. H. MacDonald, T. Jungwirth, V. K. Dugaev, and J. Sinova, "Anomalous Hall effect in a two-dimensional Dirac band: The link between the Kubo-Streda formula and the semiclassical Boltzmann equation approach," *Phys. Rev. B* **75**, 045315 (2007).
- ¹⁸B. Malaman, G. Venturini, and B. Roques, "New ternary stannides: MMn_6Sn_6 ($M = \text{Sc}, \text{Y}, \text{Sm}, \text{Gd-Tm}, \text{Lu}$) and ScFe_6Sn_6 ," *Mater. Res. Bull.* **23**, 1629–1633 (1988).
- ¹⁹S. Cheng, B. Wang, I. Lyalin, N. Bagués, A. J. Bishop, D. W. McComb, and R. K. Kawakami, "Atomic layer epitaxy of kagome magnet Fe_3Sn_2 and Sn-modulated heterostructures," *APL Mater.* **10**, 061112 (2022).
- ²⁰H. P. Rooksby and B. Lewis, "Relations between the structures of phases in the system platinum-molybdenum," *J. Less-Common Met.* **6**, 451–460 (1964).
- ²¹D. M. Clatterbuck, R. J. Lange, and K. A. Gschneidner, Jr., "Magneto-optical properties of RMn_6Sn_6 ($R = \text{Gd}, \text{Tb}, \text{Dy}, \text{Ho}, \text{Er}, \text{Tm}, \text{Lu}$) single crystals," *J. Magn. Magn. Mater.* **195**, 639–645 (1999).
- ²²W. P. Davey, "Precision measurements of the lattice constants of twelve common metals," *Phys. Rev.* **25**, 753 (1925).
- ²³J. M. Taylor, A. Markou, E. Lesne, P. K. Sivakumar, C. Luo, F. Radu, P. Werner, C. Felser, and S. S. Parkin, "Anomalous and topological Hall effects in epitaxial thin films of the noncollinear antiferromagnet Mn_3Sn ," *Phys. Rev. B* **101**, 094404 (2020).
- ²⁴D. Hong, N. Anand, C. Liu, H. Liu, I. Arslan, J. E. Pearson, A. Bhattacharya, and J. Jiang, "Large anomalous Nernst and inverse spin-Hall effects in epitaxial thin films of kagome semimetal Mn_3Ge ," *Phys. Rev. Mater.* **4**, 094201 (2020).
- ²⁵D. Khadka, T. R. Thapaliya, S. Hurtado Parra, J. Wen, R. Need, J. M. Kikkawa, and S. X. Huang, "Anomalous Hall and Nernst effects in epitaxial films of topological kagome magnet Fe_3Sn_2 ," *Phys. Rev. Mater.* **4**, 084203 (2020).
- ²⁶Y. Cheng, S. Yu, M. Zhu, J. Hwang, and F. Yang, "Tunable topological Hall effects in noncollinear antiferromagnet $\text{Mn}_3\text{Sn}/\text{Pt}$ bilayers," *APL Mater.* **9**, 051121 (2021).
- ²⁷K. Fujiwara, Y. Kato, H. Abe, S. Noguchi, J. Shiogai, Y. Niwa, H. Kumigashira, Y. Motome, and A. Tsukazaki, "Berry curvature contributions of kagome-lattice fragments in amorphous Fe–Sn thin films," *Nat. Commun.* **14**, 3399 (2023).
- ²⁸T. R. Thapaliya, T. Yoo, S. Hurtado Parra, N. D. Arndt, R. Need, J. M. Kikkawa, H. Kim, and S. X. Huang, "High-quality epitaxial thin films of topological kagome metal CoSn by magnetron sputtering," *Appl. Phys. Lett.* **119**, 201902 (2021).
- ²⁹K. Fuchs, "The conductivity of thin metallic films according to the electron theory of metals," *Math. Proc. Cambridge Philos. Soc.* **34**, 100–108 (1938).
- ³⁰E. H. Sondheimer, "The mean free path of electrons in metals," *Adv. Phys.* **1**, 1–42 (1952).
- ³¹A. Misra, M. F. Hundley, D. Hristova, H. Kung, T. Mitchell, M. Nastasi, and J. D. Embury, "Electrical resistivity of sputtered Cu/Cr multilayered thin films," *J. Appl. Phys.* **85**, 302–309 (1999).
- ³²Y. Tian, L. Ye, and X. Jin, "Proper scaling of the anomalous Hall effect," *Phys. Rev. Lett.* **103**, 087206 (2009).